Journal of Volcanology and Geothermal Research 443 (2023) 107918

Contents lists available at ScienceDirect

Journal of Volcanology and Geothermal Research

journal homepage: www.journals.elsevier.com/journal-of-volcanology-and-geothermal-research

Remote volcano monitoring using crowd-sourced imagery and Structure-from-Motion photogrammetry: A case study of Oldoinyo Lengai's active pit crater since the 2007–08 paroxysm

Pierre-Yves Tournigand [a,*], Benoît Smets [a,b], Kate Laxton [c], Antoine Dille [b], Lydéric France [d,e], Gilles Chazot [f], Cristy Ho [g], Christelle Wauthier [g,h], Emma J. Nicholson [c], Charles Happe Kasanzu [i], Maruvuko Msechu [j], Matthieu Kervyn [a]

[a] Department of Geography, Vrije Universiteit Brussel, Pleinlaan 2, Brussels 1050, Belgium
[b] Department of Earth Sciences, Royal Museum for Central Africa, Tervuren B-3080, Belgium
[c] Department of Earth Sciences, University College London, London, UK
[d] Université de Lorraine, CNRS, CRPG, Nancy F-54000, France
[e] Institut Universitaire de France (IUF), France
[f] Université de Bretagne Occidentale, Brest, France
[g] Department of Geosciences, The Pennsylvania State University, USA
[h] Institute for Computational and Data Sciences, ICDS, The Pennsylvania State University, USA
[i] School of Mines and Geosciences (SoMG), University of Dar es Salaam, P.O. Box 35052, Tanzania
[j] Tanzania Mining Commission, P.O. Box 81, Dodoma, Tanzania

ARTICLE INFO

Keywords:
Crater morphology
Photogrammetry
UAS
Oldoinyo Lengai
Monitoring
DEM

ABSTRACT

Active volcanic craters are highly dynamic geological features that undergo morphological changes on a broad range of spatial and temporal scales. Such changes have implications for the stability of the edifice, the eruptive style and the associated hazards. However, monitoring the morphological evolution of active craters at high spatial resolution and over long periods of time can be challenging, especially at remote volcanoes. In this study, we demonstrate the potential of Structure-from-Motion Multi-View Stereo photogrammetry technique based on crowd-sourced data, applied to the case study of Oldoinyo Lengai (OL) volcano in northern Tanzania. Following the 2007–08 paroxysm, OL volcano resumed its characteristic effusive activity and started to fill in with lava the newly-formed 300 m wide and 130 m deep pit crater. Monitoring capability is limited at OL due to its location in a remote non-urbanized area, therefore, the eruptive and morphological evolution is poorly constrained (*e.g.,* lava emission rates, number of vents, location of unstable areas), with hazard implications for tourists visiting the summit area. Here we use crowd-sourced images, including Unoccupied Aircraft System (UAS) images, ground-based videos and pictures collected between October 2014 and June 2022, to reconstruct high-resolution topographic time-series of OL's summit crater. With these data, we have generated 7 Digital Elevation Models (DEMs) of OL's pit crater spanning the past 8 years, and estimated the emitted volume of lava and the corresponding time averaged discharge rates (TADR). From this we characterize the geomorphological evolution of OL pit crater since the 2007–08 paroxysm and perform a preliminary hazard assessment of the crater area. InSAR COSMO-SkyMed and Sentinel-1 data covering the periods 2013–2014 and 2018–2019 were also used in this study to complement our observations. Our results indicate that the main location of lava emission within the crater floor has repeatedly shifted over the years and that the 2008 cone has experienced a subsidence over time. OL's TADR has increased over the years, reaching values one order of magnitude higher in the period 2021–2022 compared to 2014–2018. Assuming similar TADR in the coming years, the crater could be filled in by lava within the next decade, leading to new lava overflows on the flanks of the volcano.

* Corresponding author.
E-mail address: pierre-yves.tournigand@vub.be (P.-Y. Tournigand).

https://doi.org/10.1016/j.jvolgeores.2023.107918
Received 6 June 2023; Received in revised form 19 September 2023; Accepted 21 September 2023
Available online 23 September 2023

1. Introduction

Active volcanic craters are highly dynamic geological features that undergo morphological changes over a wide range of spatial and temporal scales (cm to km and hours to years, respectively). This topographic evolution has many implications for the stability of the edifice, the eruptive style, and the location and number of vents. Monitoring these changes is crucial to mitigate the numerous associated hazards, and yet is challenging for remote volcanoes or small-scale morphological variations. As a consequence of the development of automated Structure-from-Motion (SfM) and Multi-View Stereo (MVS) algorithms, ground and airborne optical imagery are increasingly being used to generate high-resolution Digital Elevation Models (DEMs), typically spanning spatial scales of a few square meters to several square kilometers (*e.g.,* James and Robson, 2012; Civico et al., 2021; Dille et al., 2021; Schmid et al., 2021). This approach is cost- and time-effective, and the spatial resolution and completeness of the DEMs depend on the quality of the acquired data (*e.g.,* image spatial resolution, adequate lighting conditions, number of images, geometry of acquisition, quality of camera-lens equipment) (Westoby et al., 2012; Fonstad et al., 2013). The SfM-MVS technique has already been applied to develop numerical fluvial models (*e.g.,* Javernick et al., 2016), to monitor the erosion of coastal cliffs (*e.g.,* James and Robson, 2012), to study landslides (*e.g.,* Lucieer et al., 2014; Dille et al., 2021), to characterize fault systems (*e.g.,* Müller et al., 2017), and to describe geysers and geothermal systems (*e.g.,* Walter et al., 2020b). It has also been used for active volcano monitoring, for example to track the evolution of volcanic domes (*e.g.,* James and Varley, 2012; Darmawan et al., 2018; Zorn et al., 2020; Carr et al., 2022), dykes (*e.g.,* Dering et al., 2019), lava flows (*e.g.,* James and Robson, 2014; Pedersen et al., 2022), or crater morphology (Hanagan et al., 2020; Walter et al., 2020a; Civico et al., 2021). To the best of our knowledge, only a few studies have used this technique to study the long-term morphological evolution of active craters (*e.g.,* Derrien et al., 2015; Hanagan et al., 2020; Barrière et al., 2022) and even fewer

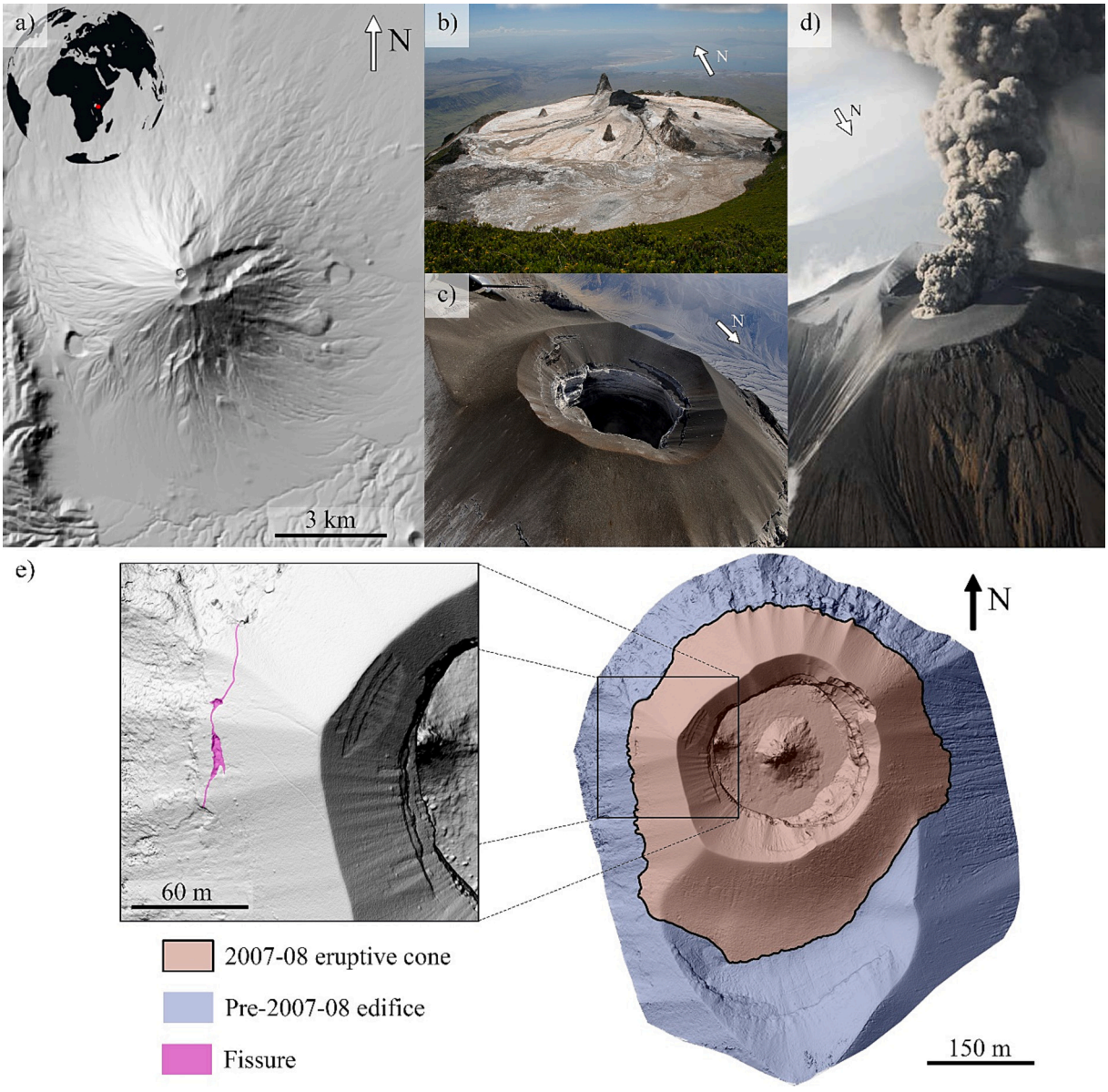

Fig. 1. Oldoinyo Lengai's a) location and hillshade of 30 m resolution SRTM DEM with overlap of July 2019 high resolution crater DEM, b) crater in May 2006 (Courtesy of Matthieu Kervyn), c) crater after the main explosive phases in March 2008 (Courtesy of Benoit Wilhelmi), d) picture of one of the main explosive phases in February 2008 (Courtesy of Benoit Wilhelmi), e) January 2021 DEM of OL summit cone, inset highlights the fissuring process on the west external slope of the cone.

performed it on a crowd-source basis (*e.g.,* Snavely et al., 2008). In this study, the term crowd-sourced data refers to open data provided by tourists and data shared through collaborations with scientists from various fields working on OL volcano. Photogrammetry can provide crucial information on volcanic activity evolution and facilitate the identification of future potential hazards (*e.g.,* lava overflow, crater wall collapse, vent migration). Photogrammetric technique relies on image acquisition and is thus applicable to both remote and highly dynamic environments, while being based on crowd-sourced data. To demonstrate the benefits of such monitoring, we apply this technique to the case study of Oldoinyo Lengai (OL) volcano, where series of images were acquired in the field by tourists and scientists without aiming at performing photogrammetric surveys.

OL is a stratovolcano (2962 m a.s.l) located in northern Tanzania. It is the only active volcano in the world to have emitted natrocarbonatite lavas historically (Keller et al., 2010). This type of emission has been ongoing at OL for at least 11 ka (France et al., 2021). Since 1983, activity at OL volcano has mostly been characterized by effusive lava emissions. However, on 4 September 2007, two explosive events marked the beginning of a new eruptive phase that persisted until April 2008 (Fig. 1). This new phase was caused by a change in magma composition, from natrocarbonatite to nephelinite melt, and involved short-lived explosive eruptions that generated volcanic ash plumes up to 15 km above vent at the peak of activity (Keller et al., 2010; Kervyn et al., 2010; Bosshard-Stadlin et al., 2014). The direct morphological consequence of this explosive phase was the formation of a pit crater, approximately 300 m wide and 130 m deep, in place of the lava platform that had filled the crater since 1983 (Kervyn et al., 2010; Laxton, 2020). Following the 2007–08 paroxysm, the deep architecture and source of the hydrothermal system has not drastically changed with respect to the pre-2007-08 paroxysm period (Mollex et al., 2018). The normal effusive activity at OL resumed and has been filling the new crater over the last 14 years, as reported through observations made sporadically by both scientists and tourists. However, due to the remote location of the volcano (120 km away from the nearest city) and the lack of scientific instruments on-site, there has been no permanent monitoring of OL's activity and crater morphology evolution. Fortunately, the uniqueness of OL volcano's natrocarbonatite as well as the neighboring points of interest (*e.g.,* Ngorongoro Lengai Geopark, Lake Natron) attract some tourists and scientists in the area, generating valuable – though relatively rare - sources of data.

Sporadic reports by tourists and visiting scientists, although mostly based on qualitative observations, provide useful information on the state of OL's activity and morphological evolution of the 2008 cone (Fig. 2). Frequent eruptive activity, characterized by small-scale intra-crater lava flows and pools, has been observed since early 2009 (Global Volcanism Program, 2013a). The formation of hornitos and the occurrence of partial crater wall collapses have also been reported (Global Volcanism Program, 2008, 2009). Crater depth has been estimated visually using a handheld laser in 2008 (130 m) and 2010 (120 m), and through photogrammetric reconstruction in 2017 (100–125 m) (Global Volcanism Program, 2008, 2010, 2018). However, these sparse data points do not allow for a quantitative analysis of the evolution of OL's crater and overall cone structure, and therefore of the intra-crater lava accumulation, eruption rates and surface displacements. In the absence of continuous *in situ* monitoring, multi-temporal high-resolution

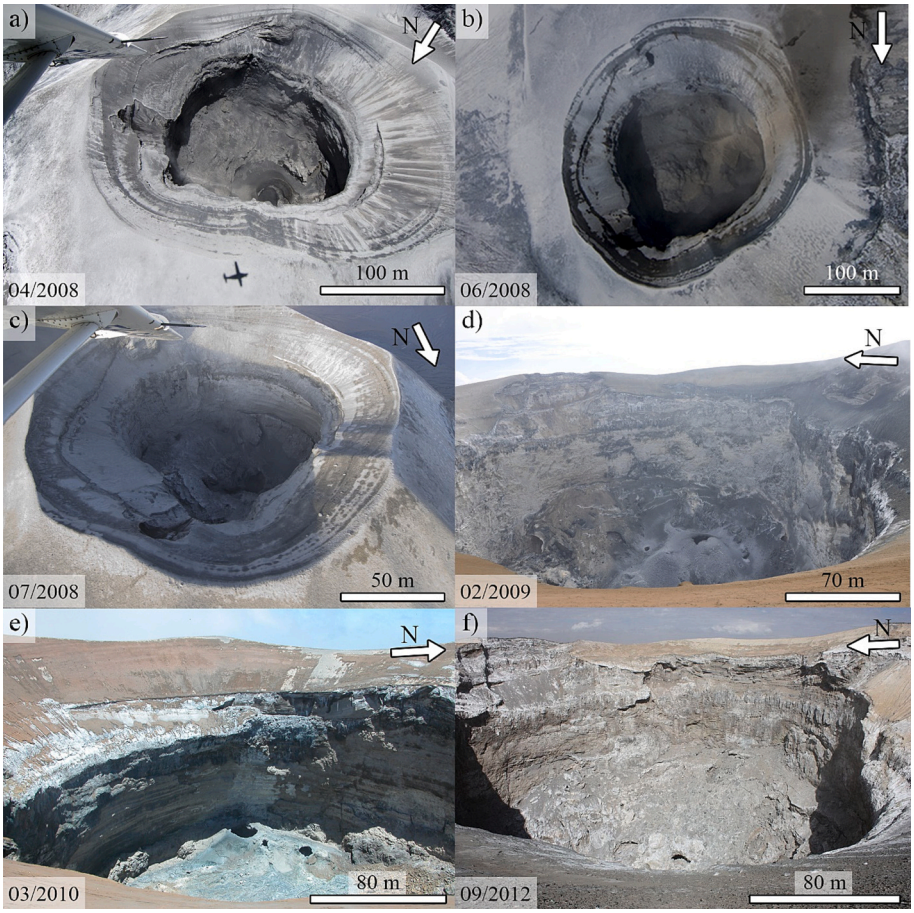

Fig. 2. Picture time-series from April 2008 to September 2012. Pictures a), b) and c) are airborne pictures acquired in April, June and July 2008, respectively (Courtesy of Benoit Wilhelmi). d) February 2009 ground-based picture (Courtesy of Ben Beeckmans). e) March 2010 ground-based picture (Courtesy of David Sherrod). f) September 2012 ground-based picture (Courtesy of Franck Mockel).

topographic reconstructions, using ground-, drone-, and aircraft-based images acquired by scientists, tourists, and pilots represent an invaluable source of data to retrieve OL's crater evolution. The difficulties in obtaining high-resolution DEMs from satellite data due to regular cloud cover and the small scale of the crater (≈ 300 m diameter) and its vent structures with respect to metric satellite data resolution further emphasize the need for more creative solutions to data acquisition. Also, higher precision measurements, such as ground-based Lidar, are not available for the period of interest. Consequently, as a complement to photogrammetric data, Interferometric Synthetic Aperture Radar (InSAR) show potential to monitor the surface displacements of the 2008 cone structure.

In this study, we demonstrate the capability of crowd-sourced photogrammetry to reconstruct a high-resolution topographic time-

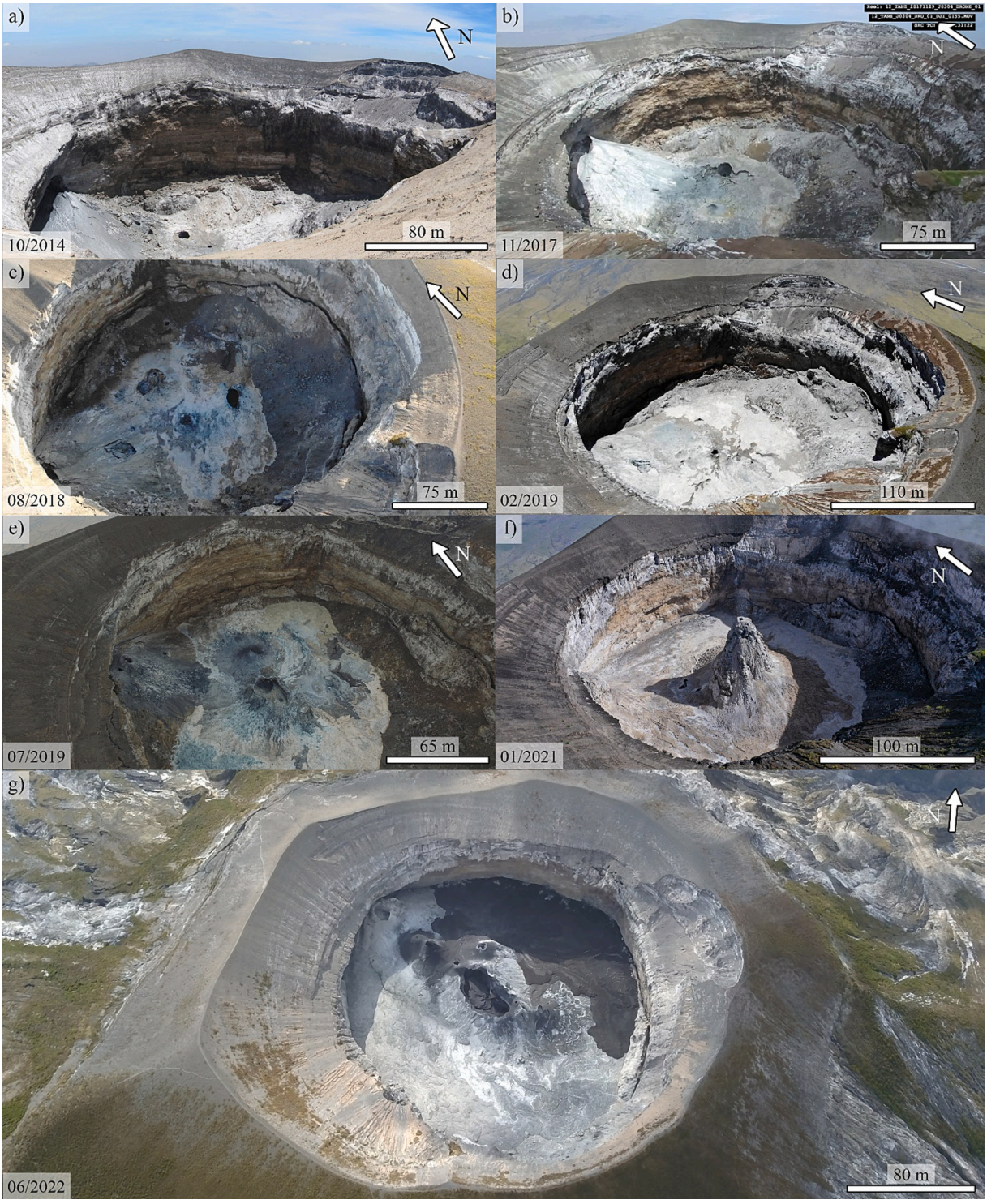

Fig. 3. Picture time-series from October 2014 to June 2022. a) October 2014 ground-based picture (Courtesy of Dr. France and Prof. Chazot), b) November 2017 UAS-based picture (Courtesy of Prof. Kervyn), c) and d) August 2018 and February 2019 UAS-based pictures, respectively (Courtesy of P. Marcel and M. Caillet), e) July 2019 UAS-based picture (Courtesy of Dr. Laxton and Dr. Nicholson), f) January 2021 UAS-based picture (Courtesy of M. Dalton-Smith and G. Schachenmann), g) June 2022 ground-based picture (Courtesy of S. Chermette).

series of the changing summit crater morphology of OL. From this time-series, we characterize the geomorphological evolution of the summit crater of OL since the 2007–08 paroxysm and assess the hazard implications. For this, we collated several sources of optical images including Unoccupied Aircraft Systems (UAS) images, videos and ground-based pictures that have been collected by scientists or tourists between October 2014 and June 2022 (Fig. 3). Using these diverse datasets, we generated 7 DEMs of OL's pit crater spanning the past 8 years and estimated the lava emitted volume and Time Averaged Discharge Rates (TADR) over time (Harris et al., 2007). Additionally, InSAR data allowed to estimate the larger scale surface displacements related to the 2008 cone.

2. Methodology

2.1. Data acquisition

One of the main challenges of this study was to gather a sufficient number of high-quality images for a given period in order to reconstruct a complete DEM of OL's active crater. The data are collated from 6 different sources and allowed the reconstruction of 7 DEMs spanning >8 years. The sensors and acquisition methods vary greatly and include pictures and videos obtained using both UAS and ground-based Digital Single Lens Reflex cameras. The motivations for each data acquisitions were also quite diverse. Some images were taken by tourists (*e.g.,* 2018), others by scientists with the objective of performing 3D reconstructions of the active crater (*e.g.,* 2017 and 2019), and some for film-making purposes (*e.g.,* 2021). UAS data were obtained by flying over and within the pit crater. Ground-based data were mostly acquired from the crater rim, except in 2014 when a GoPro camera, fixed on a cable going across the crater, was used to descend inside the structure.

Various media sources were explored to collect these datasets. First, Global Volcanism Program bulletin reports for OL were reviewed to identify individuals who had climbed or flown over the crater since 2008. Each person was contacted individually to assess those with potentially useful data for photogrammetric reconstruction. Additionally, extensive research was carried out on social media platforms (*e.g.,* YouTube, Facebook, Twitter) to identify other individuals or groups who had visited for tourism. The collected data were sorted and some periods were not used due to insufficient numbers of pictures (*i.e.,* 2008, 2010 and 2012, Fig. 2). Detailed information on the data used to reconstruct the 7 OL DEMs are presented in Table 1.

2.2. Data processing

Some images had to be extracted prior to the 3D reconstructions. Part of the data for the years 2014, 2017, 2018 and 2019 were video-based, recorded using UAS or hand-held cameras. Frames were extracted from the videos and a selection made to ensure as many different viewing geometries and as much images overlap as possible on a case by case basis.

2.2.1. Photogrammetric 3D reconstruction

The 3D reconstruction was performed using Agisoft Metashape Pro v. 1.7.2 (AMP), a SfM-MVS photogrammetry software. The reconstructions were obtained following the procedure described in James and Robson (2014), James et al. (2017) and Delhaye and Smets (2021). The first processing step is an image quality control to detect and remove images that would negatively impact the quality of the 3D reconstruction (*e.g.,* blurred and badly exposed images). The AMP image quality estimation tool was used for that purpose, and all images having a score lower than 0.7/1 were discarded. The value provided by this tool is based on the sharpness level of the most in-focus part of the picture. An image with a score inferior to 0.5/1 is recommended to be excluded from the data processing by the AMP user manual. This 0.7/1 threshold was arbitrarily set to improve the quality of the dataset while avoiding missing the necessary image overlap and view angles to perform a proper 3D reconstruction.

The next step is the image alignment, *i.e.,* image matching and interior/exterior orientation estimation. The output is a point cloud made of tie points (*i.e.,* points visible on at least two images), called sparse point cloud (SPC), and the estimation of the interior orientation parameters, called "camera calibration" in AMP. To improve the interior/exterior orientation, the SPC was filtered using filtering options provided by the software and an optimization of the camera calibration. These filters are based on specific metrics that allow the operator to remove the less precise tie points. A full description of these filters is provided in the AMP user manual (https://www.agisoft.com/downloads/user-manuals/).

After georeferencing (see 2.2.2), a dense matching is performed to produce a dense point cloud (DPC) representing the full 3D reconstruction product. The DPC is eventually cleaned up manually on its edges and where clusters of useless points are located. The cleaned DPC of each available periods (epoch) is finally used to produce a DEM (Fig. 4). Further processing information are available in the table S1 of the supplementary material.

Table 1
Properties of the pictures used for DEM reconstructions.

Year	Month	Dates	Cameras	Nb pictures	Resolution (px)	GPS geotagging	Source	Institution
2014	Oct	12 to 14	GoPro Hero3+ Black edition	46	1920 × 1080	No	Dr. France and Prof. Chazot	Université de Lorraine and Université de Bretagne Occidentale
			Nikon D7000	12	4928 × 3264			
			Information unavailable	8	4000 × 3000			
			Kodak EasyShare DX7590	14	2576 × 1716			
2017	Nov	29 to 30	DJI Phantom 4	344	1920 × 1080	No	Prof. Kervyn	Vrije Universiteit Brussels
2018	Aug	4	DJI Mavic Pro	151	1920 × 1080	No	Patrick Marcel and Marc Caillet	–
2019	Feb	28	DJI Mavic Pro	190	1920 × 1080	No		
2019	Jul	29 to 31	DJI Phantom 3 Pro	146	4000 × 3000	Yes	Dr. Laxton and Dr. Nicholson	University College London
			Canon PowerShot SX740 HS	79	5184 × 3888			
2021	Jan	24	DJI Mavic 2 Pro	80	5472 × 3648	Yes	Michael Dalton-Smith and Gian Schachenmann	–
2022	Jun	24 to 27	DJI Mavic Pro	93	4000 × 2250	Yes	Sylvain Chermette	–
			Sony Alpha 7 III	64	6000 × 4000			

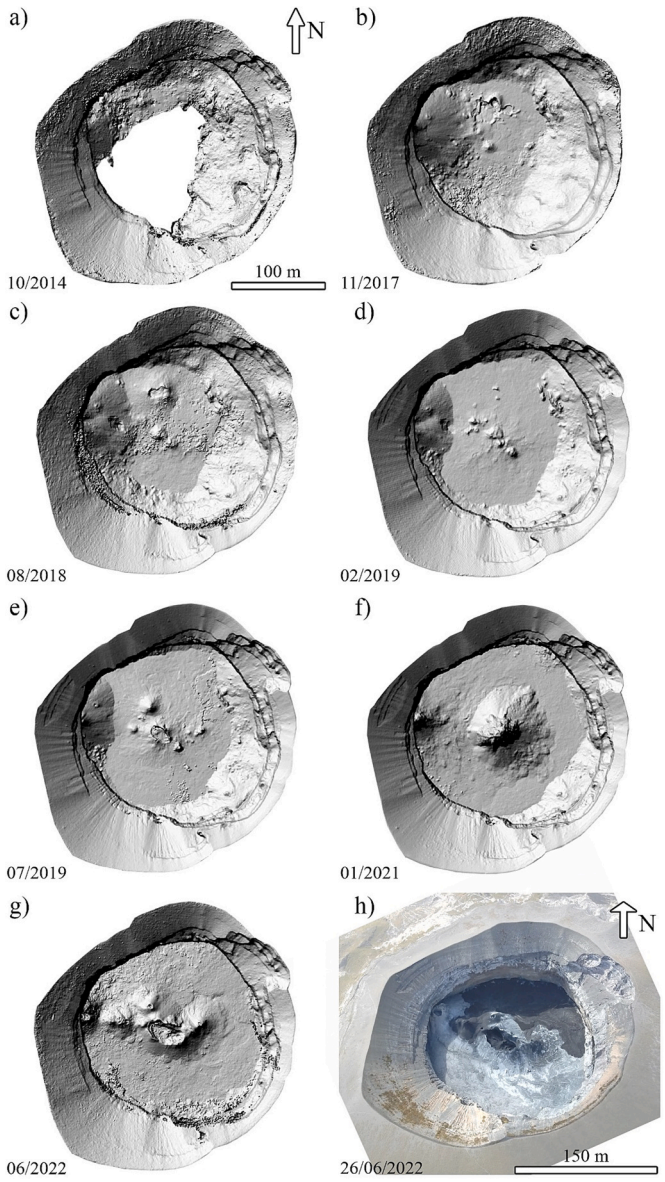

Fig. 4. Overview of the 7 DEMs reconstructed in this study: a) October 2014, b) November 2017, c) August 2018, d) February 2019, e) July 2019, f) January 2021, g) June 2022. The bottom right picture, taken on 26th of June 2022, shows the current state of OL's crater morphology (Courtesy of Sylvain Chermette).

2.2.2. Georeferencing

None of the 7 datasets included ground control points (GCPs) and 4 had no associated GPS data, yet georeferencing is essential for cross-model comparison. To perform such comparison, we used a reference epoch having a good quality of image acquisition and geotagging information. The precision of this geotagging is equivalent to a unique consumer-grade GNSS receiver (*i.e.,* 5 to 10 m), but provides centimeter- to decimeter-scale precision for an accurate scaling of the model. The reference epoch is the July 2019 dataset. It offers the best spatial resolution available in the time-series, with images acquired during ideal lighting conditions (*i.e.,* no extreme light-shadow contrasts, good visibility and exposure highlighting well the ground surface texture). As the type of image, geometry of acquisition and conditions of illumination significantly differ between epochs, multi-epoch co-alignment during the photogrammetric processing, as commonly suggested for an accurate co-registration (*e.g.,* Feurer and Vinatier, 2018; Hendrickx et al., 2020; Delhaye and Smets, 2021), was not possible. Consequently, we used the fully processed reference epoch July 2019 to manually extract the coordinates of 10 reference points visible in the final 3D products and use these points as GCPs for the other epochs. Each of these points is associated with a recognizable feature within OL's crater that could be identified easily in all the other epochs. It allowed for a co-registration of all available epochs in our dataset.

To assess the quality of the co-registration, we used the CloudCompare M3C2 plugin (Lague et al., 2013; Girardeau-Montaut, 2016). For each DPC, regions assumed to be stable around the crater were selected and compared to the reference July 2019 model. These DPC samples correspond to cone slopes with no evidence of volcanic activity (*e.g.,* tephra accumulation, collapse) or vegetation. The use of cone slopes to assess the co-registration enables both vertical and horizontal registration (Delhaye and Smets, 2021). Results are reported in Table 2.

All the co-registration differences are between 0.1 and 1.1 m with an average standard deviation of 0.3 m. These results indicate that all elevation changes measured between DEMs superior to 1.5 m are significant and correspond to real elevation changes in the pit crater. This value is conservative and is lower for all dates but August 2018.

2.2.3. Depth and volume change estimates

Parameters related to the morphology of the crater (*e.g.,* depth, surface, volume) as well as to the dynamics of the activity have been extracted from the DEM time-series (Fig. 4).

The DEMs were subtracted from each other to map the elevation differences across the entire crater area (Fig. 5) allowing both a qualitative and quantitative appraisal of OL crater morphological evolution.

As OL crater rim elevation is constant in time but variable around the crater, with minimum and maximum elevation around 2887 and 2908 m in the W-NW and S-SE area respectively, the average rim altitude (2895 m) was retrieved from the July 2019 reference model and used as the crater rim elevation.

The crater depth has been retrieved by manually contouring and measuring the average elevation of the young lava platform (*i.e.,* crater floor elevation) in each DEM, which was then subtracted from the average crater rim elevation.

The crater volume is the volume of lava needed to completely fill OL's crater. This parameter was obtained by measuring the empty volume below a virtual platform at the average crater rim elevation. Using the obtained crater volume, we derived the TADR in m^3/month:

$$TADR = \frac{|V_2 - V_1|}{t_2 - t_1} \quad (1)$$

with V_2 and V_1 being the crater volumes of two successive epochs and $t_2 - t_1$ the time difference between the two epochs of interest.

In order to retrieve the error associated to Volume and TADR calculations it was first necessary to verify the error distribution in the M3C2 results. Quantile-Quantile (Q-Q) plots were used to identify potential deviation from a normal distribution (supplementary material Fig. S1). A strong deviation from a straight line was observed indicating a non-normal distribution of the error. We thus followed the same procedure as in Höhle and Höhle (2009) and Pedersen et al. (2022) consisting in using the Normalized Median Absolute Deviation (NMAD) an estimate for standard deviation less sensitive to outliers in the datasets, to estimate the error associated to Volume and TADR estimates:

$$\sigma_V = A \bullet NMAD \quad (2)$$

where σ_V is the Volume uncertainty and A is the area that experienced an elevation change.

$$\sigma_{TADR} = \frac{A}{t_2 - t_1}\sqrt{NMAD_1{}^2 + NMAD_2{}^2} \quad (3)$$

where $t_2 - t_1$ is the time difference between 2 DEMs.

Table 2
3D reconstruction properties.

DEM	Ground resolution (cm/px)	RMS reprojection error (m)[a]	Max reprojection error (m)	Average co-registration difference (m)	Average co-registration standard deviation (m)
2014	13.88	0.22	5.31	0.11	0.51
2017	23.76	0.34	18.33	0.73	0.31
2018	20.97	0.20	6.30	1.11	0.38
2019 Feb	28.93	0.17	2.05	0.46	0.24
2019 Jul	11.87	0.25	0.89	NaN	NaN
2021	21.36	0.21	0.70	0.40	0.22
2022	18.54	0.21	0.56	0.64	0.39

[a] The RMS reprojection error is provided by the Agisoft Metashape software and correspond to the root mean square of normalized reprojection error.

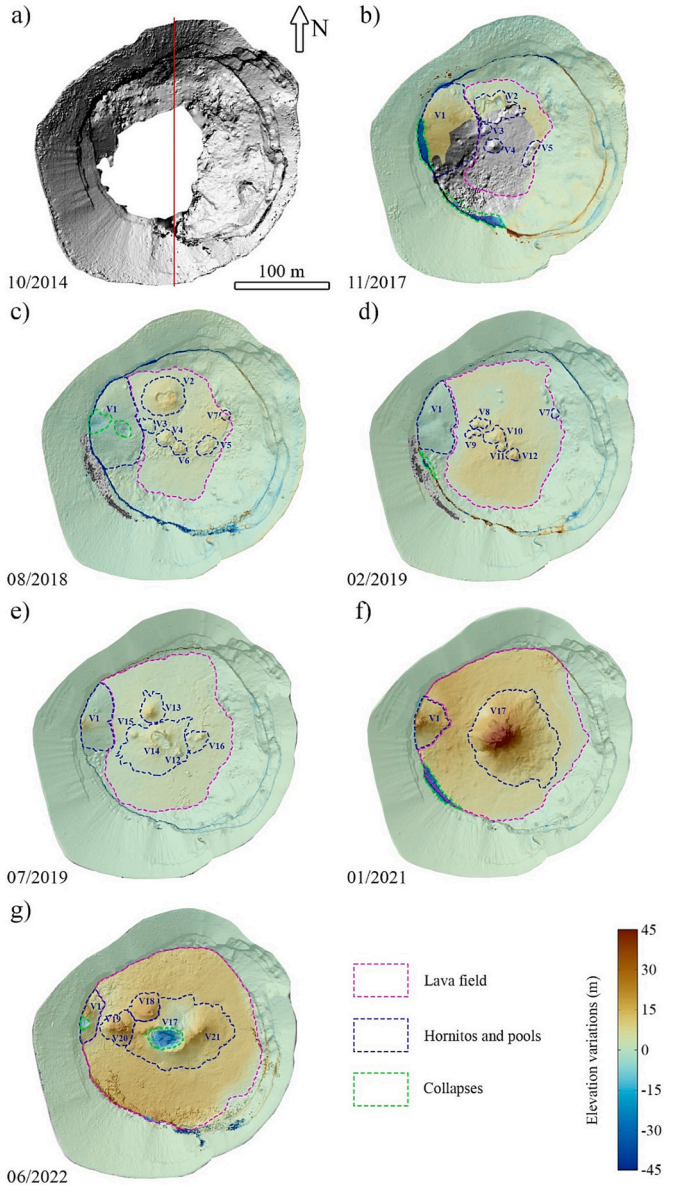

Fig. 5. Morphological evolution of OL's crater obtained by DEM subtraction: a) October 2014 DEM, b) November 2017 – October 2014, c) August 2018 – November 2017, d) February 2019 – August 2018, e) July 2019 – February 2019, f) January 2021 – July 2019, g) June 2022 – January 2021. In each case, the colormap of elevation differences is overlapping the most recent DEM: b) November 2017, c) August 2018, d) February 2019, e) July 2019, f) January 2021 and g) June 2022. The red line corresponds to the N-S profiles presented in Fig. 6a. (For interpretation of the references to colour in this figure legend, the reader is referred to the web version of this article.)

2.3. Surface displacements (InSAR data)

Surface displacements have also been quantified using InSAR to provide insights on the larger scale motion of the 2008 cone. Surface displacements were quantified using differential InSAR on three SAR datasets: 100 descending COSMO-SkyMed X-band (wavelength = 3.1 cm) SAR images spanning 2 February 2013–28 November 2014 provided by the Italian Space Agency (ASI), 35 descending Sentinel-1C-band (wavelength = 5.55 cm) SAR images spanning 21 July 2018–12 January 2020, and 44 ascending Sentinel-1C-band SAR images spanning 25 July 2018–4 January 2020 provided by the Alaska Satellite Facility (ASF). The COSMO-SkyMed dataset was multi-looked at 5 looks in range and 5 looks in azimuth, while the Sentinel-1 datasets were multi-looked at 10 looks in range and 2 looks in azimuth. 510 descending COSMO-SkyMed interferograms were made using a baseline threshold of 200 m and a maximum of 200 days between acquisitions. A baseline threshold of 300 m and a temporal threshold of 50 days were used to generate 95 descending and 162 ascending Sentinel-1 interferograms. Differential InSAR processing and unwrapping were completed using the GAMMA software (Werner et al., 2000). Topographic phases were removed using a digital elevation model of OL edifice with a 12 m spatial resolution from TanDEM-X (Krieger et al., 2007).

Cumulative surface displacement maps and time-series of displacements were generated using the Multidimensional Small Baseline Subset (MSBAS) version 3, a software that uses the least squares method on a differential InSAR dataset to produce one-dimensional Line-Of-Sight (LOS) time-series, or a combination of ascending and descending datasets to produce two-dimensional, vertical and horizontal east-west, time-series (Samsonov, 2019). Compared to conventional InSAR, MSBAS can detect smaller ground displacements over longer timespans and has been successfully used to analyze deformation related to volcanic processes (Samsonov and d'Oreye, 2012; Smets et al., 2013; Stephens and Wauthier, 2022; Gonzalez-Santana et al., 2022). The areas of interest at the crater were sampled at 10 × 10 pixels (120 m × 120 m). The InSAR time-series reference (10 × 10 pixels) is centered on the location of the OLO3 GPS station (−2.754°, 35.871°) from the TZVOLCANO GNSS Network (Stamps et al., 2016). The location is relatively stable based on GPS time-series spanning 2016–2021, which is detrended using MIDAS (Blewitt et al., 2018) and available through the Nevada Geodetic Laboratory database. No GPS data are available from 2013 to 2014, so we assume that the location of station OLO3 was also stable during this period for consistency.

3. Results

The explosive activity that took place between September 2007 and April 2008 excavated a 130 m deep pit crater, around which a new pyroclastic cone formed and now sits atop the older active platform (Fig. 1c and e). The pyroclastic cone is easily distinguishable from the older structures due to its smooth texture (Fig. 1e). In this study, the pit crater within the cone is divided into two sections, a steep-sided inner crater (≈ 200 m diameter) from the crater floor to 2866 m elevation that

will be referred to as the lower crater section and a wider upper section (≈ 300 m diameter) from 2866 to 2895 m elevation with a slope mainly at the repose angle with an average angle of 33°, referred to as the upper crater section (Fig. 6a). The lower crater section is approximately circular while the upper crater section is slightly elongated in the NE-SW direction. The upper crater section displays several features on the inner eastern slopes corresponding to collapses that occurred in the months following the paroxysm (Fig. 2). On the external section of the cone, one of the most noticeable features on our DEMs is the ≈ 100 m long fissure running parallel to the cone base on the western slopes (Fig. 1e).

Since 2014, OL's crater has undergone further significant morphological changes, including progressive filling of the crater with new lava, hornitos growth and collapses, and partial collapses of the crater walls (Fig. 5). We describe the main features of each of these processes in the sections below. For clarity, vents or clusters of vents are referred to using an associated number (*e.g.,* V1, V2, …; Fig. 5). When a vent does not significantly change location or size, its name is carried out to the next time step. On the other hand, if the location and/or dimension of a vent has changed, if several vents merged, or if vents are visible in an area previously devoted of any vent then a new name is attributed to it.

3.1. Crater filling

3.1.1. Lava field

The progressive filling of the crater is clearly visible throughout the 2017 to 2022 reconstructed DEMs, distinguishable from the smooth unaltered texture that the fresh lava generates (Fig. 5, dashed purple contours). In 2017, a young lava field is noticeable in the north and central part of the crater at a depth of 110 m, relative to the average crater rim elevation (Fig. 3b and Fig. 5b). A large hornito in the west (V1) and four main vents (V2–5) are identified, including a 12 m diameter lava pool (V2). In 2018, the lava field displays a 27% increase in surface area and a 3–4 m increase in elevation (107 m depth) with respect to 2017 (Fig. 5c and Table 3). Several vents are observed, including a lava pool (V5) on the eastern part of the field. The pool was active at the time of data acquisition. In both 2017 and 2018, the active vents are located in the northern half of the lava field. From February 2019 onwards, all active vents appear confined to the center of the lava field, which had expanded in area by 50% and increased in elevation by 4–5 m (99 m depth) with respect to August 2018 (Fig. 5d). A similar vent layout is noticeable in July 2019 with 5 active structures (V12–16) developing in the center of the field (Fig. 5e). The main structure (V14) consists of an elliptical pool measuring 24 × 14 m along its major and minor axis, respectively. The lava field surface area expanded by a further 14% with respect to the previous DEM, while its depth relative to the crater rim decreased to 97 m. Between July 2019 and January 2021, the active vents continued to converge towards the center of the crater, resulting in the formation of a single tall hornito (V17) measuring 55 m in height relative to the crater floor level (88 m depth) (Fig. 3f). A 30% increase in the lava field surface area is also observed during this time period (Fig. 5f). In June 2022, the main central hornito collapsed creating a *E*-W elongated lava pool (V17) associated with several secondary vents (V18–21) aligned in the same orientation (Fig. 5g). The lava field surface area increased by 14% and its average elevation reached 2822 m (73 m depth), almost entirely covering the remnants of V1 hornito. Cumulatively, between 2017 and 2022, the lava field surface increased from 8.4×10^3 m^2 to 2.7×10^4 m^2, while its average elevation rose by 37.2 m (from 2785.2 to 2822.4 m, respectively). Furthermore, a E-W alignment of the active vents appears from 2018 and remains visible until 2022.

3.1.2. Hornitos

A west emission center (V1) is noticeable in every DEM (Fig. 5). V1 formed a hornito located against the western crater wall (Fig. 5b). Between 2014 and 2017, this structure increased in volume, as shown by the yellow/orange colour scale in Fig. 5b. The volume change of the entire hornito cannot be constrained for each time period as the central lava field progressively covered the base of the hornito and some crater wall collapses exposed parts that were previously hidden. We therefore measured the change in the maximum height of the hornito's peak area between 2017 and 2022. From November 2017 to August 2018, V1 falls by 3.5 m in maximum elevation (Fig. 5b, c). These changes in elevation are accounted for by 2 collapses that can be distinguished in Fig. 5c, one at the V1 summit and one on the eastern side closer to its base. Between August 2018 and February 2019, V1 decreased by a further 2.3 m in maximum elevation. In July 2019, V1 exhibits an increase in maximum elevation of 5.3 m followed by an increase in maximum elevation of 24.8 m by January 2021 (Fig. 5e and f). From January 2021, V1 continued to grow, albeit at a slower rate, however its maximum elevation dropped by 1.8 m by June 2022. Fig. 5g shows that by June 2022 V1's summit has again collapsed and instead exhibits a growth around 10 m to the north.

Until February 2019, large scale hornitos and lava pools such as V2 (> 1000 m^2) formed predominantly in the northern part of the crater, while the central part only contained small-scale structures, such as V3–12 (< 300 m^2). All the vent structures were low in elevation relative to the average elevation of the crater floor (<10 m). By February 2019, all vents were confined to the central part of the crater and remained relatively small low elevation edifices (V9–12). From July 2019, larger structures developed (>10 m), all in the central region of the crater. These structures included a large collapsed hornito (V14) and several smaller ones (V12, 13, 15 and 16). Within the V14 collapsed structure, we observe several active vents characterized by a notable *E*-W alignment. In all the DEMs presented in this study, no active vent was observed in the southern part of the crater. By January 2021, all vents coalesced into one central 55 m tall hornito (V17) with a basal diameter of ≈ 90 m, for a total volume of 6.6×10^4 m^3. The structure subsequently collapsed, and 5 vents (V17–21) opened around it, forming a network of smaller scale hornitos (≈ 15 m high; Fig. 5g). From January 2021 onward, the vent structures (V17–21) grew further to reach higher elevations (> 20 m) compared to previous years and started resembling the structures observed during the 2000–2008 period (Fig. 1) (Kervyn et al., 2008).

3.1.3. Crater volume evolution

A time series of crater depth was obtained by measuring the average elevation of the young natrocarbonatite lava platform in each DEM. In October 2014, a substantial portion of the lava field is missing due to the incomplete DEM. In this case, the average elevation along the margin of the missing area's contour was used as a depth estimate, assuming a horizontal topography. OL's crater depth has been decreasing at different rates over time (Fig. 6a). Two main trends are observed, one for the period between October 2014 and August 2018 during which the crater depth decreased by ≈ 9 m, corresponding to 0.2 m/month, and the second between August 2018 and June 2022, during which the crater depth decreased by ≈ 34 m, corresponding to a higher rate of 0.7 m/month (Fig. 6b).

The first trend is in good agreement with previous crater depth measurements acquired in 2010 (Global Volcanism Program, 2010). Conversely, the depth value obtained in 2008 (Global Volcanism Program, 2008) appears higher than expected compared to the data presented here. However, one should remember that, due to the cone-shaped morphology of the original crater following the 2007–08 paroxysm, it is expected that the crater depth decreased at a faster rate in the years immediately following the resumption of effusive activity.

The remaining volume of the crater was measured for each available DEM using the average crater rim elevation as a reference (Fig. 6c). It is important to note that debris from crater wall collapses that have occurred over the studied period fell inside the crater and consequently do not impact the overall volume evolution estimation. Crater volumes were estimated at 3.5×10^6 m^3 in 2014 compared to 2.6×10^6 m^3 in

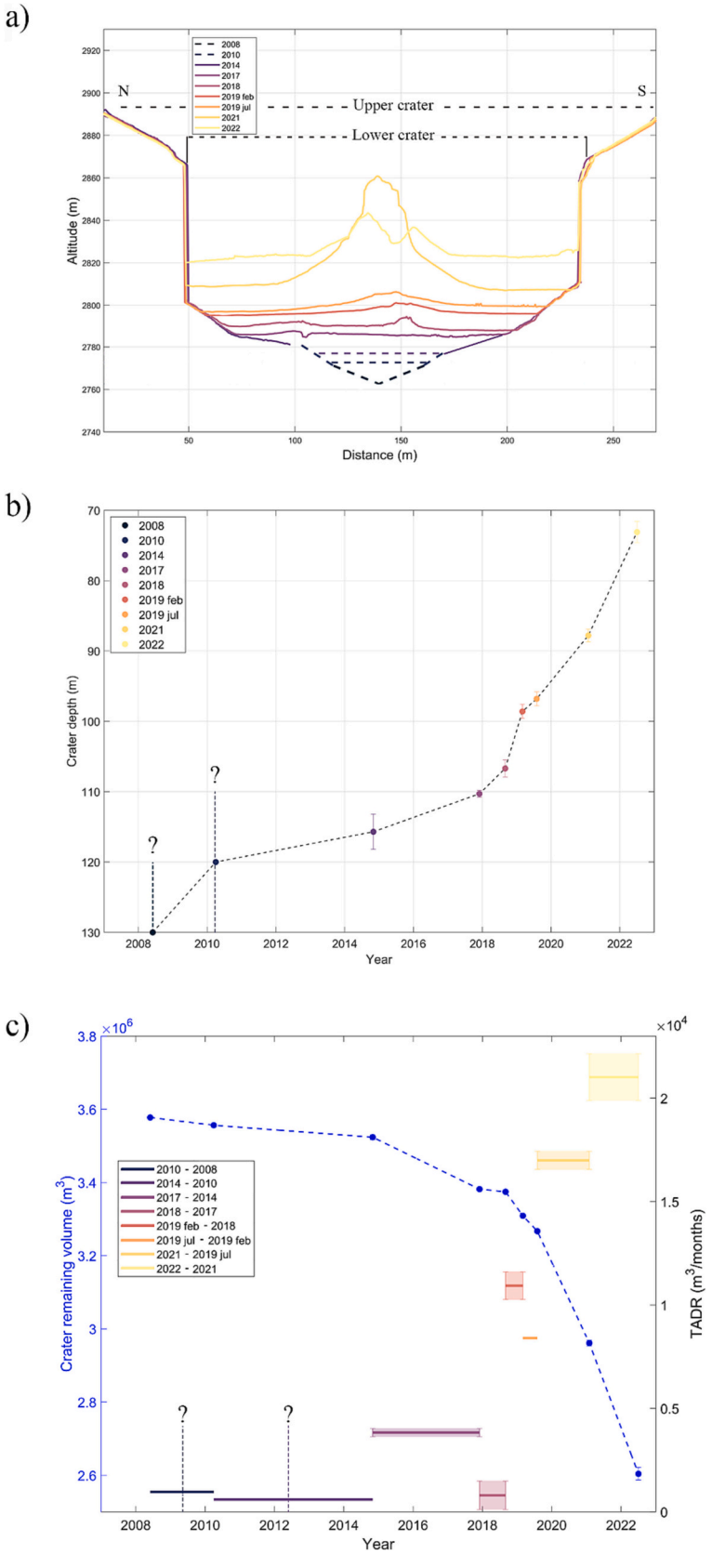

(caption on next page)

Fig. 6. a) N-S profile of each reconstructed DEM (Profile drawn on Fig. 5a). Purple dashed line represents the base level used to fill in the October 2014 missing data. Blue and dark blue dashed lines represent the assumed shapes used to estimate the 2010 and 2008 crater volumes, respectively. B) Crater depth evolution over time. Dark blue and blue colors correspond to estimates performed by Chris Weber in 2008 and David Sherrod in 2010, respectively (Global Volcanism Program, 2008, 2010). The error associated with these measurements is unknown and represented by the error bar with a question mark. C) Crater remaining volume (blue dashed line, blue axis) and emission rate (solid lines, black axis) evolution over time (shaded areas correspond to the error). Error bars associated to the crater volume estimate are displayed but in most cases are comprised within the size of the data point. (For interpretation of the references to colour in this figure legend, the reader is referred to the web version of this article.)

Table 3
Parameters extracted from DEMs and field estimates.

Years	Depth (m)	Lava field area (m^2)	Crater volume (m^3)	σ_V (m^3)	TADR (m^3/month)	σ_{TADR} (m^3/month)	Months
2008	130*	NaN	3.58E+06*	NaN	NaN	NaN	NaN
2010	120*	NaN	3.56E+06*	NaN	9.60E+02*	NaN	22
2014	115.7	NaN	3.52E+06	6.42E+03	6.00E+02	NaN	55
2017	110.3	8392	3.38E+06	4.60E+03	3.80E+03	1.98E+02	37
2018	106.7	10,679	3.37E+06	3.02E+03	8.00E+02	6.85E+02	9
2019 Feb	98.6	15,887	3.31E+06	2.82E+03	1.10E+04	6.65E+02	6
2019 Jul	96.8	18,062	3.27E+06	NaN	8.40E+03	NaN	5
2021	87.8	23,417	2.96E+06	7.81E+03	1.70E+04	4.34E+02**	18
2022	73.1	26,728	2.60E+06	1.73E+04	2.10E+04	1.13E+03	17

Note. Depth = Crater depth with respect to average lava platform and crater rim elevation, Crater volume = Volume available below a plane at the crater rim elevation, Months = number of months elapsed with respect to previous DEM, NaN = Not a Number (No data available).
* 2008 and 2010 depth values come from estimates determined by Chris Weber and Dr. David Sherrod, respectively (Global Volcanism Program, 2008, 2010).
** This σ_{TADR} uncertainty value could not be calculated based on the described method and thus was obtained by dividing σ_V by the number of months elapsed between July 2019 and 2021 surveys.

2022 corresponding to a 26% volume decrease in 8 years. As for the crater depth, two evolution trends are observed in the volume data. The first trend (from October 2014 to August 2018) shows that the crater lost ≈ 4% of its volume in almost 4 years. In comparison, the crater volume decreased by a further 23% between August 2018 and June 2022. The TADRs highlight the same two distinct evolutions over time with an initial steady low emission ($< 6 \times 10^3$ m^3/month) trend pre-2018 followed by a constantly increasing trend reaching a maximum emission rate of 2.1×10^4 m^3/month by June 2022.

We estimated the pit crater volume for the years 2010 and 2008. In these years the floor of the pit crater had a cone shape (Fig. 2a and c) that got rapidly filled over time. In the absence of DEMs for these years, the 2014 crater volume was used as a reference to which we added a supplementary volume calculated separately. To calculate the 2010 supplementary volume, the average slope of the northern region of the lower crater section was measured on the reconstructed 2014 DEM to be 27.3°. This slope value was then used to derive a truncated cone volume (Fig. 6a, blue dashed lines) below the 2014 lava field area. For 2008, a supplementary cone volume was added with a diameter equivalent to the 2010 truncated cone and a tip reaching the depth measured in 2008 (Fig. 6a, dark blue dashed lines). The corresponding TADR results showed in Fig. 6c for the periods 2008–2010 and 2010–2014 are consistent with a steady low emission period pre-2018.

3.2. Collapses

Several crater wall collapses occurred in 2017, February 2019 and 2021 (Fig. 5, dashed green contours). These collapses developed on the top of the lower crater section, in the W to SW sectors, at an average elevation of 2866 m. Each wall collapse is distinguished by the dark blue shaded areas in Fig. 5, indicating an elevation change after the collapse >45 m. This change agrees with the altitude difference between the top of the lower crater section and the crater floor in the three cases (81 m in 2017, 69 m in 2019 and 58 m in 2021). Furthermore, we observe the presence of meter-size blocks on the crater floor below the collapsed area. These collapse areas extend several tens of meters in length scale and appear to be restricted geographically to the southwestern walls of the lower crater section.

3.3. Cone subsidence

The InSAR data provided us with cumulative surface displacement maps supporting subsidence at the cone relative to the surrounding area (Fig. 7). LOS displacements of the northern (A) and southern (B) flanks both have linear rates of −3.4 cm/year according to the descending COSMO-SkyMed dataset spanning February 2013 – November 2014. Simultaneously processing the ascending and descending Sentinel-1 datasets spanning July 2018 – January 2020 yields both vertical and horizontal displacements. The northern (A), southern (B), western (C), and eastern (D) flanks have vertical displacement linear rates of −2.0, −1.0, −1.3, −0.6 cm/year, respectively, and horizontal displacement linear rates of −0.6, −0.6, −0.5, −0.4 cm/year, respectively. The biannual cyclic patterns, which are especially apparent in the vertical and horizontal displacement time-series, correspond to the wet seasons that occur in the periods March – May and October – December, when the ground swells with rainwater (Rey et al., 2021).

4. Discussion

4.1. Morphological evolution and shallow plumbing system

Numerous morphological changes are observable over time within the crater formed by the 2007–08 eruption at Oldoinyo Lengai. A new natrocarbonatite lava platform has developed, progressively covering the older formations and filling the crater (Fig. 5). We show that, within this platform the location of the active centers migrates over time from the northern region of the crater towards the center. This observation suggests subsurface changes in the geometry of OL's shallow plumbing system feeding lava emission at the surface. This interpretation is supported by other morphological changes including the formation and destruction of pools and hornitos on the lava platform. It appears that the largest structures were localized in the north part of the crater prior to July 2019, after which, large-scale structures developed solely within the center of the platform. This behavior indicates that the lava flux has been progressively redirected towards the center of OL's crater and has remained stable in this area since. This observation is confirmed by the data presented in Reiss et al. (2023) that show a thermal signal localized in the central part of the crater during the year 2019. The observed vent alignment on the DEMs also suggests an *E*-W oriented shallow feeding

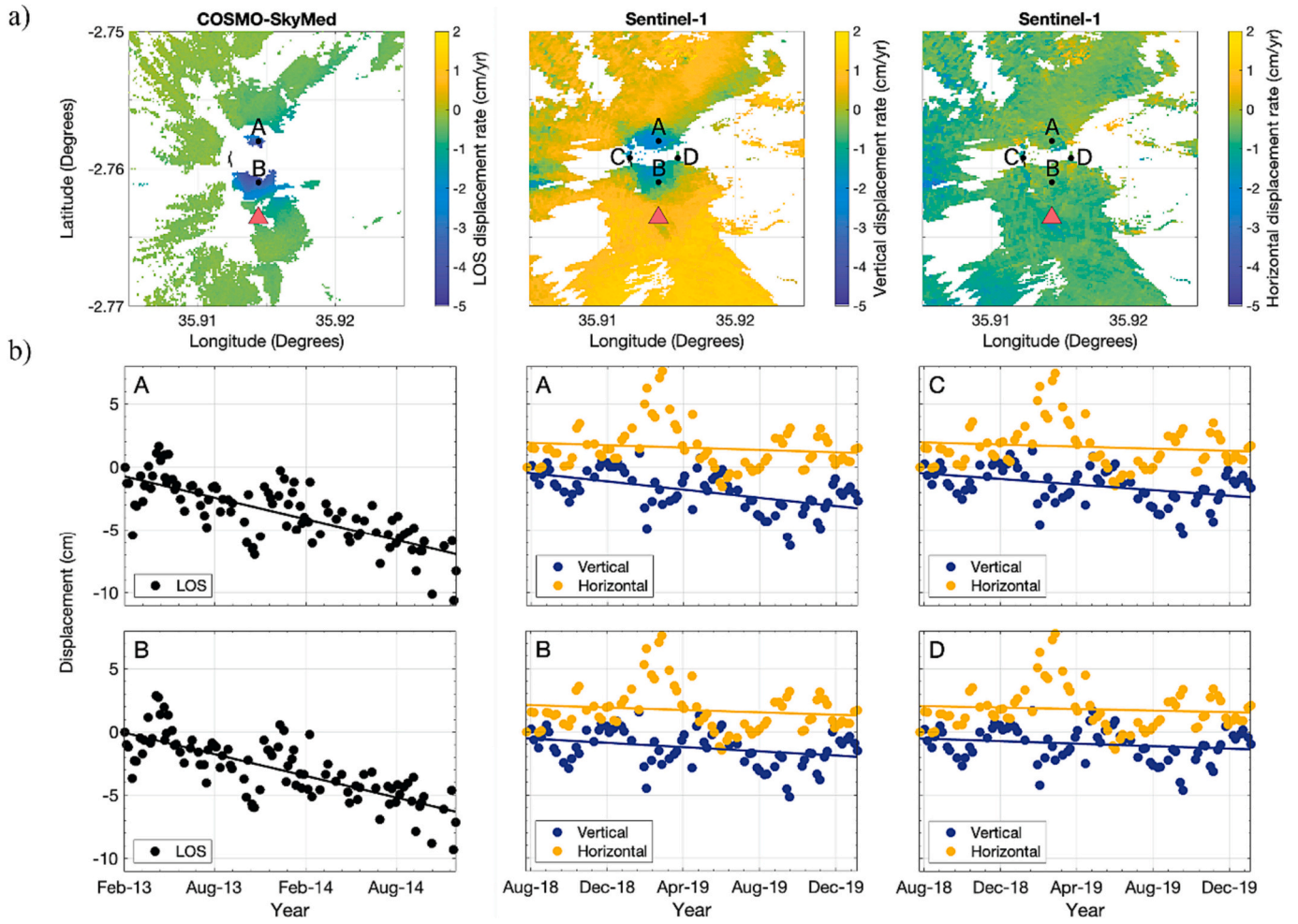

Fig. 7. a) Cumulative surface displacement maps from COSMO-SkyMed (February 2013 – November 2014) and Sentinel-1 (July 2018 – January 2020) data and b) time-series plots for points A through D. The red triangle represents the Oldoinyo Lengai summit, and the black outline represents the observed fissure on the western cone flank. The InSAR time-series reference coordinates are −2.754°, 35.871°. (For interpretation of the references to colour in this figure legend, the reader is referred to the web version of this article.)

system. Interestingly, Kervyn et al. (2008) made similar observations of vent alignments at OL but oriented in a N-S direction at that time. Kervyn et al. (2008) also reported very shallow interconnected magma reservoirs directly below the collapsed remnants of large hornitos structures, as observed in June 2022. We also observe an evolution in the eruptive style at OL over time. Vent structures were low in elevation (<10 m) prior to January 2021. This suggests an eruptive activity composed mostly of lava flows as it will tend to direct the flux in the main slope direction and propagate over a long distance (several tens of meters). On the other end, our data suggest that the more recent activity has been dominated by spattering that favor a radial short range distribution of the erupted products, hence allowing the formation of higher structures.

These observations tend to indicate that an E-W feeding system has been created or reactivated in OL's pit crater and that the magma flux has been migrating through this system and increasing over time. A potential explanation for an E-W oriented feeding system is related to the morphology of OL summit area. The 2008 cone rests on a relatively flat platform composed of natrocarbonatites formed north of the summit over the last century (Klaudius and Keller, 2006). The southern part of the 2008 cone is bounded by the topography of the volcano's summit which provides stability to the cone structure. On the other hand, the northern part of the cone is directly built up on lava flows accumulated (Fig. 2 in Klaudius and Keller, 2006) on the northern edge of that flat platform overlying the steep outer flank (Fig. 1c, d and e). Furthermore, fumaroles are regularly observed on the upper flanks of the volcano, especially close to the 100 m fissure on the west part of the 2008 cone and on the northern flanks, likely generating an alteration of the natrocarbonatites in these areas. Such differences of stability between the northern and southern parts of the 2008 cone could impact the stress field within the pit crater, favoring N-S extension stress field that would favor an *E*-W oriented feeding system at shallow level.

The central part of the crater is one of two primary regions of localized eruptive activity in OL's crater. An active vent on the western edge of the crater (V1) has been active since before October 2014. Fig. 2e displays a view of the western side of the crater in March 2010. At that time the western hornito (V1) was not formed but a small cone with a large vent at its summit is visible. This structure is most likely one of the first stages of V1 formation. From November 2017 until at least February 2019, V1 stopped emitting, before reactivating. Interestingly, the activity of the central lava field and the vent V1 appear to be anti-correlated (Fig. 5). During the 6 months period August 2018 – February 2019 when V1 was in quiescence, the lava field volume increased by $\approx 8.4 \times 10^4$ m^3, twice as much as during the 9 months period November 2017 – August 2018. During the 5 months period February 2019 to July 2019 the lava field volume only increased by $\approx 5.2 \times 10^4$m^3, when V1 was being reactivated. Thermal InfraRed satellite data confirm V1 reactivation by showing an absence of thermal signal on the western part of OL's crater between March and May 2019 and then the presence of a hotspot in June 2019 (Reiss et al., 2023). After this, V1

appears to be quiescent again at least until March 2020 according to MSI-Sentinel 2 and OLI-Landsat 8. However, we can observe that V1 increased again in volume in January 2021 and June 2022 indicating a new activation of the vent between March 2020 and January 2021. From July 2019, the lava field volume steadily increased again until June 2022. It appears that lava emission at the western vents ceased while the central vents were migrating from the northern part to the central region of the crater from November 2017 to February 2019. From February 2019 onwards, both areas were active simultaneously. After the merging of all central vents into one main hornito (V17) in January 2021, OL's crater displayed only two main active vents, the central (V17) and western (V1) vents (Fig. 5f). In June 2022, we show that the number of vents increased again and spread along an E-W axis between the central and west active areas. We explain this observation by considering that the collapse of V1 and V17's summits likely clogged their main conduits. The result of this is a stress distribution change within the hornitos plumbing systems, consequently forcing lateral magma migration and the formation of new vents in the vicinity of V1 and V17 (Fig. 5g).

Temporal vent migration, successive vent activation and deactivation as well as simultaneous emission from multiple vents is well known and regularly observed at other open vent volcanoes, including Stromboli in Italy and Yasur in Vanuatu (Nabyl et al., 1997; Oppenheimer et al., 2006; Harris and Ripepe, 2007; Gaudin et al., 2014, 2017; Simons et al., 2020). This phenomenon is often explained by interconnected conduits and shallow reservoirs typically no more than a few hundred meters deep, *e.g.,* ≈ 300 m depth in the case of Stromboli volcano (Harris and Ripepe, 2007). Despite further geophysical constraints on OL's deep plumbing system (Reiss et al., 2022), substantial knowledge gaps remain regarding its shallow plumbing system. It has been suggested in Kervyn et al. (2008) that vent migrations at OL were related to extremely shallow magma reservoirs (*i.e.,* few tens of meters depth). The observed shifts in active area within OL's crater suggest regular reconfiguration of the shallow plumbing system associated to the formation and clogging of preferential eruption pathways between magma storage and surface. Thermal erosion is also a phenomenon observed at OL that could play a significant role in the motion of active vents (Dawson et al., 1990; Kervyn et al., 2008). It also appears that higher hornitos, associated with spattering, form when less vents are active. It could be explained by the flow being concentrated on fewer vents, hence, building a higher pressure.

The overall TADR at OL exhibits a steady increase since August 2018, culminating at 2.1×10^4 m^3/month (8×10^{-3} m^3/s) in June 2022. Over the past 4 years, the TADR was 7 times greater than the average value obtained for the steady period 2010–2018 (10^{-3} m^3/s), in good agreement with previously documented emission rates of 2×10^{-3} m^3/s reported by Dawson et al. (1990). A distinct change in the TADR has occurred during the studied period, with a stable, low rate in the period 2010–2018 and an increasing rate in the period 2018–2022. Thus, it appears that somewhere between August 2018 and February 2019, OL volcano experienced a change in its magma feeding system that modified both the lava flux and the conduit geometry. This is a crucial finding with a direct implication on the remaining time before a new overflow event may initiate.

4.2. Instabilities

At least 4 major crater wall collapses took place during the studied period, 2 during the period October 2014 – November 2017, 1 between August 2018 and February 2019 and 1 between July 2019 and January 2021. The presence of meter-size blocks accumulated on the crater floor in these areas confirms the occurrence of these events. Collapses appear restricted to the SW crater wall and we explain this in the context of the crater geometry. The observed collapses affect the sub-vertical walls of the lower part of the crater. While most of the steep-sided walls of the crater are vertical, in the SW region, the crater walls are overhanging with an angle of ≈ 70° to the horizontal. These overhanging crater walls are therefore less stable than the rest of the lower crater section. Based on images taken during and after the 2007–08 paroxysm we can see that the newly formed crater experienced multiple collapses (Fig. 2). These collapses appear to have taken place mostly in the eastern and northern sections of the crater, some of which impacted the crater up to its upper section. Based on our data we know that these collapses occurred between July 2008 and February 2009. Interestingly, climbers reported hearing "strong thundering noises" and sensed tremors on 12 October 2008, while being close to the summit (Global Volcanism Program, 2009). Thick steam from the crater was also reported on 26 October 2008. These two events could be related to the aforementioned collapses. The northern and eastern pit crater walls have remained stable since. However, in the case of the SW overhanging walls, it took many years to collapse. One possible explanation could be that the activity migration from the north to the center of the crater over the years, together with the increase in TADR, have generated new instabilities within OL crater through shaking and fracturing.

An additional sign of instability is noted on the outer part of the cone formed in 2008, where a 100 m long-fissure formed on the western flank very close to the contact between the newly formed cone and previous deposits (Fig. 1e). Based on our dataset and previous studies, we can confirm that this fissure dates back to at least 2013 (Global Volcanism Program, 2013b). This feature presents a future potential hazard. Should this fissure weakens the integrity of the cone, the flanks could ultimately fail and generate collapse within the pit crater. This would be a significant hazard for any climbers on the edifice at that time. No clear evolution of the fissure is observable over the years in our data but observations on the field suggest that the fissure is getting larger. Based on our DEM comparison, the overall crater flanks and inner walls do not show any motion that could be related to it. However, the InSAR data clearly indicate a subsidence of the 2008 cone area (Fig. 7). This subsidence appears to be of larger magnitude during the February 2013 – November 2014 period with a displacement of ≈ −3.4 cm/year compared to the period July 2018 – January 2020 with a vertical displacement between −0.6 and − 2.0 cm/year. The observed surface displacement is most certainly a gravitational subsidence that can potentially be associated with a ring fault system as observed at Sierra Negra (Amelung et al., 2000; Jónsson et al., 2005; Jónsson, 2009), Tendürek (Bathke et al., 2013) and Okmok (Johnson et al., 2010) volcanoes. The decrease of subsidence rate between the periods February 2013 – August 2014 and August 2018 – December 2019 could be partially related to the increase of filling rate observed since 2018 that is limiting inward dipping movement by stabilizing the inner crater wall. Furthermore, the western flank fissure could result from this subsidence and is likely accommodating some of it. The fissure could indeed be related to a destabilization of the young cone towards the pit crater. Considering that the SW walls of the lower crater section display a 70° inclination to the horizontal and that the 100 m fissure on the outer part of the cone covers the west area, we could assume that these two features are related. These features could be part of a slow destabilization of the western flank of the cone towards the pit crater. No motion of the western flank towards the crater's center is observed with the DEM comparison which could be explained if the said motion is very slow (< 2–3 cm/month).

4.3. Historical behavior and future implications

Phases of effusive natrocarbonatite emissions refilling progressively OL's crater, as observed over the past decade, have been described repeatedly in the recent history of this volcano. The 1917, 1966 and 2007 paroxysmal eruptions were all preceded by several years of effusive activity confined to the crater (Dawson et al., 1968; Nyamweru, 1990; Dawson et al., 1995; Kervyn et al., 2010). Progressive filling of the crater led to lava overflows and, ultimately, to the lava platform being removed by violent explosive activity. During these effusive phases, the formation and destruction of large hornitos (or needles) have also been

reported, for example in 1910, a 40 to 50 m tall hornito located on the northern rim of the crater (Dawson et al., 1995) and in 2006, a 60 m tall hornito located at the northwest overflow (Global Volcanism Program, 2006). Migration in the location of active vents and the opening of new vents have been described extensively at OL (*e.g.,* Dawson et al., 1994; Global Volcanism Program, 2013a). The TADRs calculated in this study are of similar magnitude to literature values from other periods (Dawson et al., 1990). A marked difference between the 2007–08 paroxysm compared to previous ones is the absence of a subsequent hiatus in OL's activity. The 1917, 1940 and 1966 paroxysmal events were followed by a quiescent period that, in some cases, lasted several years (Dawson et al., 1995; Kervyn et al., 2010). It is however important to remain careful with this information as the number of observations historically may not have been as numerous as in recent years and the lack of observational tools (*e.g.,* thermal cameras, satellite, UAS) may have limited the detection of activity and contributed to an observational bias.

If the 2022 emission rate (Table 3) is sustained in the coming years, the crater lower section could be filled within 5 years allowing again climbers to go down in OL's crater. About 8.7 years would be required for the crater floor to reach once again the crater rim's lowest elevation point (2887 m in the W-NW area) and to have natrocarbonatite overflow the crater onto the outer flanks. However, assuming an increasing emission rate following the same trend it has since 2018, the crater could be filled in as little as 6 years.

In terms of hazard implications, further collapses at the level of the lower crater section are to be expected in the coming years, especially in the SW area, until the lower section is filled with lava. Indeed, the overhanging walls of this crater section are likely to be still unstable. Once the lower section has been filled and the lava level approaches the crater rim, hazards for climbers will include hornitos and crater floor collapses as well as small-scale explosions and lava flows. Comprehensive management plans and scenario-based risk assessments will be required to safely manage volcano tourism. Lava overflows may resume at OL once the lava platform reaches the crater rim level, as previously reported prior to the 1917 and 2007 paroxysms. These overflows will most likely take place in the W-NW area of the crater where the rim elevation is lowest. As this is the area where the current climbing path is reaching the crater rim, any lava overflow could potentially disturb or prevent reaching the summit with the current path. Finally, the 2008 cone stability should be monitored in the future as we observed a subsidence of the whole structure over the years and the presence of a fissure on the western flank. It is important to follow this evolution in the coming years to anticipate potential destabilization of the cone leading to flank collapses.

Although data collected as part of this study do not allow us to get insights into when OL volcano may experience a new paroxysm, based on the knowledge gained from past events, the time span between two paroxysms varies from 9 to 40 years. With only 15 years having elapsed since the last paroxysm, OL is therefore still towards the lower end of inter-eruption period duration. It is also important to highlight that even the maximum TADR of 2.1×10^4 m^3/month remains an order of magnitude lower with respect to the estimate of 2×10^5 m^3/month obtained for August 2007, just prior to the 2007–08 paroxysm (Kervyn et al., 2010). Despite this, the recent dynamic evolution of OL's shallow plumbing system and the abrupt increase in emission rate emphasize the need to monitor this volcano closely and regularly – even through simple photographic techniques.

4.4. The potential in crowd-sourced data

In this study, we evidence the potential that resides in videos and pictures captured by volcanologists, locals and tourists, to not only document visual changes in activity but also to reconstruct quantitatively the morphological evolution of a remote volcanic crater where *in situ* monitoring is challenging and therefore limited. This study also highlights the value of open collaboration between scientists from different fields, allowing this study to benefit from other researchers' field work by getting access to data acquired for other purposes than photogrammetry.

The use of crowd-sourced data is becoming increasingly common and has recently enabled the reconstruction of the chronology of the 2013 eruption of San Miguel volcano, El Salvador (Brown et al., 2022). The addition of crowd-sourced data revealed phenomena that would not have been detected based on analysis of the deposits alone (Brown et al., 2022). Technological development over the past two decades has provided most individuals with miniaturized cameras (phones, compact cameras) and this becomes a crucial data source for scientists, especially at remote and unmonitored volcanoes such as in East Africa (Fontijn et al., 2018; Biggs et al., 2021). The drawback of such data is the added complexity of pre-processing and integration. These data are not acquired under the same conditions (point of view, lighting conditions, number of images, camera type), have different properties, and thus can be challenging to compile in a coherent dataset for photogrammetric analysis and comparison. For example, several retrieved datasets in this study were inadequate and we were unable to reconstruct DEMs at sufficiently high resolution (2008, 2010 and 2012). Another, DEM turned out incomplete, *i.e.,* the 2014 DEM. However, in most cases it was possible to produce high-resolution DEMs accurately co-registered. Although the data were from various origins, robust quantitative assessments of crater depth, lava surface areas and emission rates were performed, providing a unique insight into the activity of OL over the years.

To further improve the results of future studies based on crowd-sourced data some straightforward and practical guidelines could be provided for locals and tourists willing to collect and share data during visits to remote volcanoes. The photogrammetric technique used in this study requires to follow only 4 basic principles. First, a minimum number of pictures is necessary depending on the size of the area of interest (in our case 80 pictures was the lower limit). Second, the pictures need to be taken from as many different viewing geometries as possible. Third, pictures need to partially overlap to facilitate the SfM-MVS processing. Fourth, the pictures need to be taken during even lighting conditions, ideally around midday to avoid shadows. Finally, for people remaining over several days, acquiring the data in the same conditions every day would facilitate comparisons.

5. Conclusion

Using crowd-sourced image data acquired at OL and analyzing these datasets with SfM-MVS, we have reconstructed 7 DEMs of the pit crater to evaluate its spatial and temporal morphological changes occurring since the 2007–08 paroxysm. Many instabilities in OL's crater are highlighted in this study, including crater walls and hornitos collapses as well as the presence of a 100 m long fracture on the western outer cone flank. Our results document several fundamental changes in the shallow plumbing system, including vent migration and a succession of active and quiet phases. We observe that OL's active vents have migrated from the northern crater area towards its center, while the southern area never displayed any activity. The vents have merged into tall hornitos before again scattering after the hornitos collapses suggesting significant changes in the stress field over time. We also observe an *E*-W vent alignment since 2019 combined with the formation of taller and larger hornitos suggesting an increase in spattering in OL eruptive style. The refill rate of the pit crater displays a permanent increase over time, with a distinct acceleration occurring since 2018 and culminating at a maximum rate of 2.1×10^4 m^3/months in 2022. Assuming a similar emission rate is maintained in the coming years, the crater could be filled entirely and start to again overflow within 8 years. Regular monitoring of the OL pit crater is therefore critical to accurately forecast its future evolution in order to mitigate the risk to nearby populations and tourists.

By combining pictures taken by tourists and scientists we were able to generate an unprecedented dataset spanning the past 8 years of activity at OL volcano. Further, this study confirmed that, when used correctly, crowd-sourced images represent an extensive and cost-effective source of data for scientists that could provide invaluable qualitative and quantitative constraints on activity at volcanoes that are not permanently monitored, such as OL. With respect to the SfM-MVS methodology, only a few criteria (pertaining to the number of images, viewing geometries, overlap and lighting conditions) must be respected to acquire useful data in the form of high-quality images. Consequently, if such information is passed on to travel agencies and local populations, this presents a collaborative opportunity to involve both community members and tourists in the acquisition and sharing of scientific data whilst at the same time promoting a forum for effective and sustained two-way knowledge exchange.

Declaration of Competing Interest

The authors declare that they have no known competing financial interests or personal relationships that could have appeared to influence the work reported in this paper.

Data availability

All the data mentioned in this article are available upon request to the first author.

Acknowledgement

The authors want to thank the contribution of Sylvain Chermette from 80 jours voyages and the Société de Volcanologie de Genève (SVG), who provided data for June 2022. We also want to thank Michael Dalton-Smith and Gian Schachenmann from Serengeti Films and Kicheche Natural History Unit, for providing us data for January 2021. We want to thank Patrick Marcel, Regis Etienne and Marc Caillet from the SVG for providing data covering August 2018 and February 2019. Finally, the authors want to thank Benoit Wilhelmi, Ben Beeckmans, David Sherrod and Franck Mockel for providing pictures of OL crater for 2008, 2009, 2010 and 2012, respectively. PYT acknowledges the support of the Research Foundation Flanders (FWO), through the MORPHEUS postdoc project (grant FWOTM996). BS was supported by the GuiDANCE project (Belgian Science Policy Office, FED-tWIN Programme, Grant Prf-2019-066). KL and EJN acknowledge funding for the July 2019 expedition through the Alfred P. Sloan Foundation's support of the Deep Carbon Observatory Deep Earth Carbon Degassing program (DECADE). CW and CH acknowledge the support from the National Science Foundation (NSF) CAREER EAR 1945417 and EAR 1923943. We also thank the Tanzania Commission for Science and Technology (COSTECH) for field permits and all the guides and porters for their help during field work. LF & GC acknowledge the support of the French National Research Agency through the national program "Investissements d'avenir" with the reference ANR-10-LABX-21-01/LABEX RESSOURCES21, and through the project GECO-REE (ANR-16-01–0003CE-01). This is CRPG contribution number 2850 and GECO-REE contribution number 8.

Appendix A. Supplementary data

Supplementary data to this article can be found online at https://doi.org/10.1016/j.jvolgeores.2023.107918.

References

Amelung, F., Jónsson, S., Zebker, H., Segall, P., 2000. Widespread uplift and 'trapdoor' faulting on Galápagos volcanoes observed with radar interferometry. Nature 407, 993–996. https://doi.org/10.1038/35039604.

Barrière, J., et al., 2022. Intra-Crater Eruption Dynamics at Nyiragongo (D.R. Congo), 2002–2021. J. Geophys. Res. Solid Earth 127. https://doi.org/10.1029/2021JB023858 e2021JB023858.

Bathke, H., Sudhaus, H., Holohan, E.p., Walter, T.R., Shirzaei, M., 2013. An active ring fault detected at Tendürek volcano by using InSAR. J. Geophys. Res. Solid Earth 118, 4488–4502. https://doi.org/10.1002/jgrb.50305.

Biggs, J., Ayele, A., Fischer, T.P., Fontijn, K., Hutchison, W., Kazimoto, E., Whaler, K., Wright, T.J., 2021. Volcanic activity and hazard in the East African Rift Zone. Nat. Commun. 12, 6881. https://doi.org/10.1038/s41467-021-27166-y.

Blewitt, G., Hammond, W., Kreemer, C., 2018. Harnessing the GPS Data Explosion for Interdisciplinary Science. Eos 99. https://doi.org/10.1029/2018eo104623.

Bosshard-Stadlin, S.A., Mattsson, H.B., Keller, J., 2014. Magma mixing and forced exsolution of CO2 during the explosive 2007–2008 eruption of Oldoinyo Lengai (Tanzania). J. Volcanol. Geotherm. Res. 285, 229–246. https://doi.org/10.1016/j.jvolgeores.2014.08.017.

Brown, R.J., Hernández, W., Escobar, D., Gutierrez, E., Crummy, J., Cole, R., Tournigand, P.-Y., 2022. Reconstruction of the 29th December 2013 eruption of San Miguel volcano, El Salvador, using video, photographs, and pyroclastic deposits. Volcanica 5, 271–293. https://doi.org/10.30909/vol.05.02.271293.

Carr, B.B., Lev, E., Vanderkluysen, L., Moyer, D., Marliyani, G.I., Clarke, A.B., 2022. The Stability and Collapse of Lava Domes: Insight from Photogrammetry and Slope Stability Models Applied to Sinabung Volcano (Indonesia). Front. Earth Sci. 10. https://www.frontiersin.org/articles/10.3389/feart.2022.813813 (accessed April 2023).

Civico, R., et al., 2021. Unoccupied Aircraft Systems (UASs) Reveal the Morphological changes at Stromboli Volcano (Italy) before, between, and after the 3 July and 28 August 2019 Paroxysmal Eruptions. Remote Sens. 13, 2870. https://doi.org/10.3390/rs13152870.

Darmawan, H., Walter, T.R., Troll, V.R., Budi-Santoso, A., 2018. Structural weakening of the Merapi dome identified by drone photogrammetry after the 2010 eruption. Nat. Hazards Earth Syst. Sci. 18, 3267–3281. https://doi.org/10.5194/nhess-18-3267-2018.

Dawson, J.B., Bowden, P., Clark, G.C., 1968. Activity of the carbonatite volcano Oldoinyo Lengai, 1966. Geol. Rundsch. 57, 865–879. https://doi.org/10.1007/BF01845369.

Dawson, J.B., Pinkerton, H., Norton, G.E., Pyle, D.M., 1990. Physicochemical properties of alkali carbonatite lavas:Data from the 1988 Eruption of Oldoinyo Lengai, Tanzania. Geology 18, 260–263. https://doi.org/10.1130/0091-7613(1990)018<0260:PPOACL>2.3.CO;2.

Dawson, J.B., Pinkerton, H., Pyle, D.M., Nyamweru, C., 1994, June. 1993 eruption of Oldoinyo Lengai, Tanzania: Exceptionally viscous and large carbonatite lava flows and evidence for coexisting silicate and carbonate magmas. Geology 22, 799–802. https://doi.org/10.1130/0091-7613(1994)022<0799:JEOOLT>2.3.CO;2.

Dawson, J.B., Keller, J., Nyamweru, C., 1995. Historic and recent Eruptive activity of Oldoinyo Lengai. In: Bell, K., Keller, J. (Eds.), Carbonatite Volcanism: Oldoinyo Lengai and the Petrogenesis of Natrocarbonatites. Berlin, Heidelberg, Springer, pp. 4–22. https://doi.org/10.1007/978-3-642-79182-6_2. IAVCEI Proceedings in Volcanology.

Delhaye, L., Smets, B., 2021. Time-Series in Structure-from-Motion Photogrammetry: Testing Co-Registration Approaches for Topographic Change Analysis. In: 2021 IEEE International Geoscience and Remote Sensing Symposium IGARSS, pp. 4648–4651. https://doi.org/10.1109/IGARSS47720.2021.9553796.

Dering, G.M., Micklethwaite, S., Thiele, S.T., Vollgger, S.A., Cruden, A.R., 2019. Review of drones, photogrammetry and emerging sensor technology for the study of dykes: Best practises and future potential. J. Volcanol. Geotherm. Res. 373, 148–166. https://doi.org/10.1016/j.jvolgeores.2019.01.018.

Derrien, A., Villeneuve, N., Peltier, A., Beauducel, F., 2015. Retrieving 65 years of volcano summit deformation from multitemporal structure from motion: the case of Piton de la Fournaise (La Réunion Island). Geophys. Res. Lett. 42, 6959–6966. https://doi.org/10.1002/2015GL064820.

Dille, A., Kervyn, F., Handwerger, A.L., d'Oreye, N., Derauw, D., Mugaruka Bibentyo, T., Samsonov, S., Malet, J.-P., Kervyn, M., Dewitte, O., 2021. When image correlation is needed: Unravelling the complex dynamics of a slow-moving landslide in the tropics with dense radar and optical time series. Remote Sens. Environ. 258, 112402. https://doi.org/10.1016/j.rse.2021.112402.

Feurer, D., Vinatier, F., 2018. Joining multi-epoch archival aerial images in a single SfM block allows 3-D change detection with almost exclusively image information. ISPRS J. Photogramm. Remote Sens. 146, 495–506. https://doi.org/10.1016/j.isprsjprs.2018.10.016.

Fonstad, M.A., Dietrich, J.T., Courville, B.C., Jensen, J.L., Carbonneau, P.E., 2013. Topographic structure from motion: a new development in photogrammetric measurement. Earth Surf. Process. Landf. 38, 421–430. https://doi.org/10.1002/esp.3366.

Fontijn, K., McNamara, K., Zafu Tadesse, A., Pyle, D.M., Dessalegn, F., Hutchison, W., Mather, T.A., Yirgu, G., 2018. Contrasting styles of post-caldera volcanism along the Main Ethiopian Rift: Implications for contemporary volcanic hazards. J. Volcanol. Geotherm. Res. 356, 90–113. https://doi.org/10.1016/j.jvolgeores.2018.02.001.

France, L., Brouillet, F., Lang, S., 2021. Early carbonatite magmatism at Oldoinyo Lengai volcano (Tanzania): carbonatite–silicate melt immiscibility in Lengai I melt inclusions: Comptes Rendus. Géoscience 353, 273–288. https://doi.org/10.5802/crgeos.99.

Gaudin, D., Taddeucci, J., Scarlato, P., Moroni, M., Freda, C., Gaeta, M., Palladino, D.M., 2014. Pyroclast Tracking Velocimetry illuminates bomb ejection and explosion dynamics at Stromboli (Italy) and Yasur (Vanuatu) volcanoes. J. Geophys. Res. Solid Earth 119. https://doi.org/10.1002/2014JB011096, 2014JB011096.

Gaudin, D., Taddeucci, J., Scarlato, P., Harris, A., Bombrun, M., Del Bello, E., Ricci, T., 2017. Characteristics of puffing activity revealed by ground-based, thermal infrared imaging: the example of Stromboli Volcano (Italy). Bull. Volcanol. 79, 24. https://doi.org/10.1007/s00445-017-1108-x.

Girardeau-Montaut, D., 2016. CloudCompare. https://www. danielgm.net/cc.

Global Volcanism Program, 2006. Report on Ol Doinyo Lengai (Tanzania). In: Wunderman, R. (Ed.), Bulletin of the Global Volcanism Network, 31:3. Smithsonian Institut. https://doi.org/10.5479/si.GVP.BGVN200603-222120.

Global Volcanism Program, 2008. Report on Ol Doinyo Lengai (Tanzania). In: Wunderman, R. (Ed.), Bulletin of the Global Volcanism Network, 33:6. Smithsonian Institution. https://doi.org/10.5479/si.GVP.BGVN200806-222120.

Global Volcanism Program, 2009. Report on Ol Doinyo Lengai (Tanzania). In: Wunderman, R. (Ed.), Bulletin of the Global Volcanism Network, 34:2. Smithsonian Institution. https://doi.org/10.5479/si.GVP.BGVN200902-222120.

Global Volcanism Program, 2010. Report on Ol Doinyo Lengai (Tanzania). In: Wunderman, R. (Ed.), Bulletin of the Global Volcanism Network, 35:5. Smithsonian Institution. https://doi.org/10.5479/si.GVP.BGVN201005-222120.

Global Volcanism Program, 2013a. Ol Doinyo Lengai (222120). In: Venzke, E. (Ed.), Volcanoes of the World, v. 4.11.0 (08 Jun 2022). Smithsonian Institution. Downloaded 14 Jun 2022. https://volcano.si.edu/volcano.cfm?vn=222120. https://doi.org/10.5479/si.GVP.VOTW4-2013.

Global Volcanism Program, 2013b. Report on Ol Doinyo Lengai (Tanzania). In: Wunderman, R. (Ed.), Bulletin of the Global Volcanism Network, 38:6. Smithsonian Institution. https://doi.org/10.5479/si.GVP.BGVN201306-222120.

Global Volcanism Program, 2018. Report on Ol Doinyo Lengai (Tanzania). In: Krippner, J.B., Venzke, E. (Eds.), Bulletin of the Global Volcanism Network, 43:10. Smithsonian Institution. https://doi.org/10.5479/si.GVP.BGVN201810-222120.

Gonzalez-Santana, J., Wauthier, C., Burns, M., 2022. Links between volcanic activity and flank creep behavior at Pacaya Volcano. Guatemala: Bull. Volcanol. 84, 84. https://doi.org/10.1007/s00445-022-01592-2.

Hanagan, C., La Femina, P.C., Rodgers, M., 2020. Changes in Crater Morphology Associated With Volcanic Activity at Telica Volcano, Nicaragua. Geochem. Geophys. Geosyst. 21 https://doi.org/10.1029/2019GC008889 e2019GC008889.

Harris, A., Ripepe, M., 2007. Synergy of multiple geophysical approaches to unravel explosive eruption conduit and source dynamics – a case study from Stromboli: Chem. Erde-Geochem. 67, 1–35. https://doi.org/10.1016/j.chemer.2007.01.003.

Harris, A., Dehn, J., Calvari, S., 2007. Lava effusion rate definition and measurement: a review. Bull. Volcanol. 70, 1–22. https://doi.org/10.1007/s00445-007-0120-y.

Hendrickx, H., De Sloover, L., Stal, C., Delaloye, R., Nyssen, J., Frankl, A., 2020. Talus slope geomorphology investigated at multiple time scales from high-resolution topographic surveys and historical aerial photographs (Sanetsch Pass, Switzerland). Earth Surf. Process. Landf. 45, 3653–3669. https://doi.org/10.1002/esp.4989.

Höhle, J., Höhle, M., 2009. Accuracy assessment of digital elevation models by means of robust statistical methods. ISPRS J. Photogramm. Remote Sens. 64, 398–406. https://doi.org/10.1016/j.isprsjprs.2009.02.003.

James, M.R., Robson, S., 2012. Straightforward reconstruction of 3D surfaces and topography with a camera: Accuracy and geoscience application. J. Geophys. Res. Earth Surf. 117 https://doi.org/10.1029/2011JF002289.

James, M.R., Robson, S., 2014. Sequential digital elevation models of active lava flows from ground-based stereo time-lapse imagery. ISPRS J. Photogramm. Remote Sens. 97, 160–170. https://doi.org/10.1016/j.isprsjprs.2014.08.011.

James, M.R., Varley, N., 2012. Identification of structural controls in an active lava dome with high resolution DEMs: Volcán de Colima, Mexico. Geophys. Res. Lett. 39 https://doi.org/10.1029/2012GL054245.

James, M.R., Robson, S., d'Oleire-Oltmanns, S., Niethammer, U., 2017. Optimising UAV topographic surveys processed with structure-from-motion: Ground control quality, quantity and bundle adjustment. Geomorphology 280, 51–66. https://doi.org/10.1016/j.geomorph.2016.11.021.

Javernick, L., Hicks, D.M., Measures, R., Caruso, B., Brasington, J., 2016. Numerical Modelling of Braided Rivers with Structure-from-Motion-Derived Terrain Models. River Res. Appl. 32, 1071–1081. https://doi.org/10.1002/rra.2918.

Johnson, J.H., Prejean, S., Savage, M.K., Townend, J., 2010. Anisotropy, repeating earthquakes, and seismicity associated with the 2008 eruption of Okmok volcano, Alaska. J. Geophys. Res. Solid Earth 115. https://doi.org/10.1029/2009JB006991.

Jónsson, S., 2009. Stress interaction between magma accumulation and trapdoor faulting on Sierra Negra volcano, Galápagos. Tectonophysics 471, 36–44. https://doi.org/10.1016/j.tecto.2008.08.005.

Jónsson, S., Zebker, H., Amelung, F., 2005. On trapdoor faulting at Sierra Negra volcano, Galápagos. J. Volcanol. Geotherm. Res. 144, 59–71. https://doi.org/10.1016/j.jvolgeores.2004.11.029.

Keller, J., Klaudius, J., Kervyn, M., Ernst, G.G.J., Mattsson, H.B., 2010. Fundamental changes in the activity of the natrocarbonatite volcano Oldoinyo Lengai, Tanzania. Bull. Volcanol. 72, 893–912. https://doi.org/10.1007/s00445-010-0371-x.

Kervyn, M., Ernst, G.G.J., Klaudius, J., Keller, J., Kervyn, F., Mattsson, H.B., Belton, F., Mbede, E., Jacobs, P., 2008. Voluminous lava flows at Oldoinyo Lengai in 2006: Chronology of events and insights into the shallow magmatic system. Bull. Volcanol. 70, 1069–1086. https://doi.org/10.1007/s00445-007-0190-x.

Kervyn, M., Ernst, G.G.J., Keller, J., Vaughan, R.G., Klaudius, J., Pradal, E., Belton, F., Mattsson, H.B., Mbede, E., Jacobs, P., 2010. Fundamental changes in the activity of the natrocarbonatite volcano Oldoinyo Lengai, Tanzania. Bull. Volcanol. 72, 913–931. https://doi.org/10.1007/s00445-010-0360-0.

Klaudius, J., Keller, J., 2006. Peralkaline silicate lavas at Oldoinyo Lengai, Tanzania. Lithos, Peralkaline Rocks 91, 173–190. https://doi.org/10.1016/j.lithos.2006.03.017.

Krieger, G., Moreira, A., Fiedler, H., Hajnsek, I., Werner, M., Younis, M., Zink, M., 2007. TanDEM-X: A Satellite Formation for High-Resolution SAR Interferometry. IEEE Trans. Geosci. Remote Sens. 45, 3317–3341. https://doi.org/10.1109/TGRS.2007.900693.

Lague, D., Brodu, N., Leroux, J., 2013. Accurate 3D comparison of complex topography with terrestrial laser scanner: Application to the Rangitikei canyon (N-Z). ISPRS J. Photogramm. Remote Sens. 82, 10–26. https://doi.org/10.1016/j.isprsjprs.2013.04.009.

Laxton, K., 2020. Collection of lava samples from Ol Doinyo Lengai. Nat. Rev. Earth & Environ. 1, 438. https://doi.org/10.1038/s43017-020-0089-z.

Lucieer, A., de Jong, S.M., Turner, D., 2014. Mapping landslide displacements using Structure from Motion (SfM) and image correlation of multi-temporal UAV photography. Progress Phys. Geograph.: Earth Environ. 38, 97–116. https://doi.org/10.1177/0309133313515293.

Mollex, G., Füri, E., Burnard, P., Zimmermann, L., Chazot, G., Kazimoto, E.O., Marty, B., France, L., 2018. Tracing helium isotope compositions from mantle source to fumaroles at Oldoinyo Lengai volcano, Tanzania. Chem. Geol. 480, 66–74. https://doi.org/10.1016/j.chemgeo.2017.08.015.

Müller, D., Walter, T.R., Schöpa, A., Witt, T., Steinke, B., Gudmundsson, M.T., Dürig, T., 2017. High-Resolution Digital Elevation Modeling from TLS and UAV Campaign reveals Structural Complexity at the 2014/2015 Holuhraun Eruption Site, Iceland. Front. Earth Sci. 5. https://www.frontiersin.org/article/10.3389/feart.2017.00059 (accessed June 2022).

Nabyl, A., Dorel, J., Lardy, M., 1997. A comparative study of low-frequency seismic signals recorded at Stromboli volcano, Italy, and at Yasur volcano, Vanuatu. N. Z. J. Geol. Geophys. 40, 549–558. https://doi.org/10.1080/00288306.1997.9514783.

Nyamweru, C., 1990. Observations on changes in the active crater of Ol Doinyo Lengai from 1960 to 1988. J. Afr. Earth Sci. 11, 385–390. https://doi.org/10.1016/0899-5362(90)90017-9.

Oppenheimer, C., Bani, P., Calkins, J.A., Burton, M.R., Sawyer, G.M., 2006. Rapid FTIR sensing of volcanic gases released by Strombolian explosions at Yasur volcano, Vanuatu. Appl. Phys. B Lasers Opt. 85, 453–460. https://doi.org/10.1007/s00340-006-2353-4.

Pedersen, G.B.M., Belart, J.M.C., Óskarsson, B.V., Gudmundsson, M.T., Gies, N., Högnadóttir, T., Hjartardóttir, Á.R., Pinel, V., Berthier, E., Dürig, T., Reynolds, H.I., Hamilton, C.W., Valsson, G., Einarsson, P., Ben-Yehosua, D., Gunnarsson, A., Oddsson, B., 2022. Volume, Effusion Rate, and Lava Transport During the 2021 Fagradalsfjall Eruption: Results From Near Real-Time Photogrammetric Monitoring. Geophys. Res. Lett. 49 https://doi.org/10.1029/2021GL097125 e2021GL097125.

Reiss, M.C., De Siena, L., Muirhead, J.D., 2022. The Interconnected Magmatic Plumbing System of the Natron Rift. Geophys. Res. Lett. 49 https://doi.org/10.1029/2022GL098922 e2022GL098922.

Reiss, M.C., Massimetti, F., Laizer, A.S., Campus, A., Rümpker, G., Kazimoto, E.O., 2023. Overview of seismo-acoustic tremor at Oldoinyo Lengai, Tanzania: Shallow storage and eruptions of carbonatite melt. J. Volcanol. Geotherm. Res. 107898 https://doi.org/10.1016/j.jvolgeores.2023.107898.

Rey, T., Leone, F., Defossez, S., Gherardi, M., Parat, F., 2021. Volcanic hazards assessment of Oldoinyo Lengai in a data scarcity context (Tanzania). Territorium 69–81. https://doi.org/10.14195/1647-7723_28-2_6.

Samsonov, S.V., 2019. User Manual, Source Code, and Test Set for MSBASv3 (Multidimensional Small Baseline Subset Version 3) for One- and Two-Dimensional Deformation Analysis, Open File 45. Natural Resources Canada, Ottawa, ON, Canada, pp. 1–13.

Samsonov, S., d'Oreye, N., 2012. Multidimensional time-series analysis of ground deformation from multiple InSAR data sets applied to Virunga Volcanic Province. Geophys. J. Int. 191, 1095–1108. https://doi.org/10.1111/j.1365-246X.2012.05669.x.

Schmid, M., Kueppers, U., Civico, R., Ricci, T., Taddeucci, J., Dingwell, D.B., 2021. Characterising vent and crater shape changes at Stromboli: implications for risk areas. Volcanica 4, 87–105. https://doi.org/10.30909/vol.04.01.87105.

Simons, B.C., Jolly, A.D., Eccles, J.D., Cronin, S.J., 2020. Spatiotemporal Relationships between Two Closely-spaced Strombolian-style Vents, Yasur, Vanuatu. Geophys. Res. Lett. 47 https://doi.org/10.1029/2019GL085687 e2019GL085687.

Smets, B., et al., 2013. Detailed multidisciplinary monitoring reveals pre- and co-eruptive signals at Nyamulagira volcano (North Kivu, Democratic Republic of Congo). Bull. Volcanol. 76, 787. https://doi.org/10.1007/s00445-013-0787-1.

Snavely, N., Seitz, S.M., Szeliski, R., 2008. Modeling the World from Internet Photo Collections. Int. J. Comput. Vis. 80, 189–210. https://doi.org/10.1007/s11263-007-0107-3.

Stamps, D.S., Saria, E., Ji, K.H., Jones, J.R., Ntambila, D., Daniels, M.D., Mencin, D., 2016. Real– time data from the Tanzania Volcano Observatory at the Ol Doinyo Lengai volcano in Tanzania (TZVOLCANO). UCAR/NCAR ÀÀÀ Earth Observing Laboratory.

Stephens, K.J., Wauthier, C., 2022. Spatio-temporal evolution of the magma plumbing system at Masaya Caldera, Nicaragua. Bull. Volcanol. 84, 18. https://doi.org/10.1007/s00445-022-01533-z.

Walter, T.R., Belousov, A., Belousova, M., Kotenko, T., Auer, A., 2020a. The 2019 Eruption Dynamics and Morphology at Ebeko Volcano Monitored by Unoccupied Aircraft Systems (UAS) and Field Stations. Remote Sens. 12, 1961. https://doi.org/10.3390/rs12121961.

Walter, T.R., Jousset, P., Allahbakhshi, M., Witt, T., Gudmundsson, M.T., Hersir, G.P., 2020b. Underwater and drone based photogrammetry reveals structural control at Geysir geothermal field in Iceland. J. Volcanol. Geotherm. Res. 391, 106282. https://doi.org/10.1016/j.jvolgeores.2018.01.010.

Werner, C., Wegmüller, U., Strozzi, T., Wiesmann, A., 2000. Gamma SAR and interferometric processing software. Proceed. Ers-Envisat Symp. 1620, 1620.

Westoby, M.J., Brasington, J., Glasser, N.F., Hambrey, M.J., Reynolds, J.M., 2012. 'Structure-from-Motion' photogrammetry: A low-cost, effective tool for geoscience applications. Geomorphology 179, 300–314. https://doi.org/10.1016/j.geomorph.2012.08.021.

Zorn, E.U., Walter, T.R., Johnson, J.B., Mania, R., 2020. UAS-based tracking of the Santiaguito Lava Dome, Guatemala. Sci. Rep. 10, 8644. https://doi.org/10.1038/s41598-020-65386-2.